Sedimentary Geology 399 (2020) 105604

Contents lists available at ScienceDirect

Sedimentary Geology

journal homepage: www.elsevier.com/locate/sedgeo

Multimineral fingerprinting of modern sand generated from the Tethys Himalaya (Nianchu River, Tibet)

Wendong Liang [a,*], Alberto Resentini [a], Ronghua Guo [b], Eduardo Garzanti [a]

[a] *Laboratory for Provenance Studies, Department of Earth and Environmental Sciences, University of Milano-Bicocca, 20126 Milano, Italy*
[b] *School of Earth Sciences and Engineering, Nanjing University, 210029 Nanjing, China*

ARTICLE INFO

Article history:
Received 1 October 2019
Received in revised form 22 January 2020
Accepted 24 January 2020
Available online 27 January 2020

Editor: Dr. Catherine Chagué

Keywords:
Tethys Himalaya
Nianchu
Petrography and heavy minerals
Erosion rate
Lithological control
Climatic control

ABSTRACT

The Nianchu, as the largest southern tributary of the middle Yarlung Tsangpo (upper Brahmaputra River in southern Tibet), drains mainly sedimentary rocks of the Tethys Himalaya and subordinately metamorphic and igneous rocks of the Greater Himalaya, Kangmar gneiss dome, and Indus-Yarlung ophiolitic suture zone. This study presents the first detailed compositional fingerprinting of detritus released from the Tethys Himalaya in southern Tibet. Sand carried by the Nianchu and by its major tributaries range from quartzo-lithic to litho-quartzose sedimentaclastic with a few metamorphic, volcanic, and ultramafic lithic grains, reflecting dominant erosion of Tethys Himalayan strata. Transparent heavy-mineral assemblages are moderately poor. They include a mixed recycled assemblage with amphibole, tourmaline and rounded zircon, together with first-cycle sillimanite and garnet grains from the Greater Himalaya, young titanite and monazite grains from either the Greater Himalaya or the Kangmar dome, chloritoid from the low-grade metapelites surrounding the Kangmar dome, and clinopyroxene, olivine and enstatite grains shed from forearc ophiolites. Forward mixing models indicate that ~80% of Nianchu sand is recycled from the Tethys Himalaya, which is roughly the same percentage as the corresponding exposure area. Based on previous geochronological and provenance studies, and on available suspended-load data from the Nianchu, Lhasa and Yarlung Tsangpo rivers, we assess the average erosion rate in the Nianchu catchment as ~0.10 mm a^{-1}, about twice as that in the middle Yarlung Tsangpo catchment (0.05 mm a^{-1}) and about five times as that of the Lhasa River catchment (0.02 mm a^{-1}). This marked difference is principally ascribed to the higher erodibility of Tethys Himalayan sedimentary strata. Within the Nianchu basin, low precipitation in the rain shadow of the high Himalayan range may explain a lower erosion rate in the headwaters (0.07 mm a^{-1}) than in the less steep lower reaches (0.14 mm a^{-1}).

1. Introduction

Orogenic belts are composed of a series of distinct tectonic domains, generally arranged roughly subparallel to tectonic strike. Each of these domains consists of an assemblage of diverse lithological units, which may generate a wide range of sediment compositions (Garzanti et al., 2007a). In order to unravel the erosional evolution of a huge orogenic belt such as the Himalayas, we need to quantitatively identify the signature of detritus derived from each one of these tectonic domains ("first order sampling scale" of Ingersoll, 1990; Garzanti et al., 2007b).

The Himalayan orogen is a thick-skinned thrust belt produced by collision between the Indian passive and Asian active continental margins along the Indus-Yarlung ophiolitic suture zone (Gansser, 1980; Hodges, 2000). The Yarlung Tsangpo (the headwater branch of the Brahmaputra River in south Tibet; *tsangpo* means big river in Tibetan language) flows eastward along the ophiolitic suture zone over a total length of 2057 km (Guan et al., 1984), and receives detritus from both the Lhasa Block in the north, representing the original Trashimalayan active margin of Neotethys (Zhu et al., 2011) and from the Tethys Himalaya in the south, representing the former passive continental margin of India facing Neotethys (Sciunnach and Garzanti, 2012).

The principal aims of this article are to illustrate the minerology of detritus generated in the Tethys Himalaya domain and to unravel the complex interplay between endogenous and exogenous controls on sediment fluxes and erosion rates.

Assessing the fingerprint of each detrital source-rock domain in an orogenic belt is a fundamental step to understand its erosional evolution (Garzanti et al., 2004). Our paper is the first one that describes in detail the compositional fingerprints of detritus released from the Tethys Himalaya in southern Tibet, thus providing a reference for comparison for any provenance studies of ancient Himalayan sandstones. The Nianchu (*chu* = water, river in Tibetan language), a relatively large river that drains northward across the entire Tethys Himalayan zone, cutting across the North Himalayan Kangmar gneiss dome (Fig. 1; Chen et al., 1990; Hauck et al., 1998; Lee et al., 2000), provides an

---

* Corresponding author.
E-mail address: w.liang@campus.unimib.it (W. Liang).

https://doi.org/10.1016/j.sedgeo.2020.105604
0037-0738/

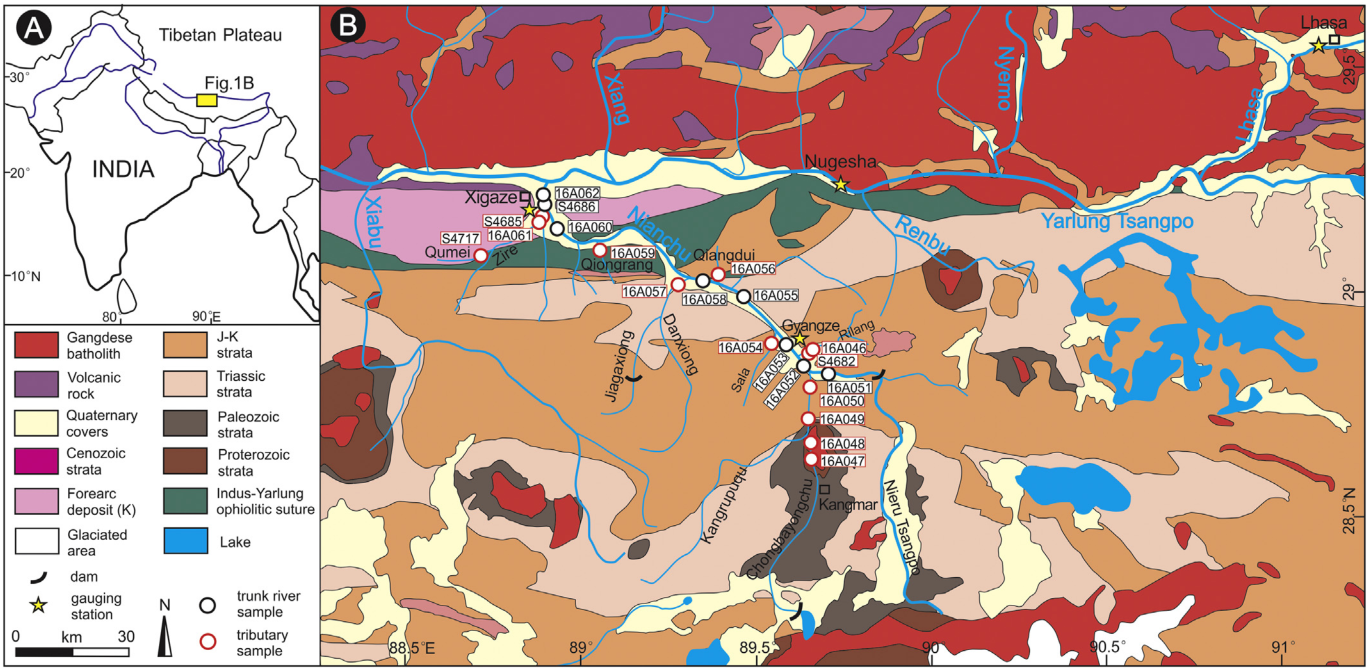

Fig. 1. Location of the study area (A) and geological setting (B) after Pan et al. (2004). Detailed information on sample locations is provided in Supplementary Table S1.

excellent natural laboratory in which to define the petrographic, mineralogical, and geochronological signatures of sediment shed today by Tethys Himalayan strata.

Unraveling the mutual interactions among climatic, geomorphological and tectonic processes remains as a major challenge in the field of orogenic research (e.g., Lavé and Avouac, 2001; Burbank et al., 2003; Godard et al., 2014). In combination with the previous provenance study of the Lhasa River (Garzanti et al., 2018) and of recent detrital geochronology work (Zhang et al., 2012; Carrapa et al., 2017; Guo et al., 2020), we can tentatively estimate the relative sediment contribution from diverse tectonic domains, trace the regional erosion patterns, better understand and disentangle the lithological (e.g. Carrapa et al., 2017; Garzanti et al., 2018) and climatic (e.g. Bookhagen and Burbank, 2006; Shi et al., 2018) influence on erosional processes.

2. Geological framework

The continental collision between India and Asia took place around 60 Ma (DeCelles et al., 2014; Hu et al., 2015, 2016). The Tethys Himalayan stratigraphic sequence (Fig. 1), representing the sedimentary succession of northernmost India (Sciunnach and Garzanti, 2012), is bounded to the north by the south-dipping Great Counter Thrust and traditionally subdivided into southern and northern zones by the Lhagoi Kangri anticline (Burg et al., 1987; Ratschbacher et al., 1994). The southern Tethys Himalaya includes platform carbonates and siliciclastic rocks of Paleozoic to Eocene age that have undergone thrust-sheet deformation and mainly very-low grade metamorphism after continental collision (Willems et al., 1996; Jadoul et al., 1998; Hu et al., 2012). Differently, the northern Tethys Himalaya includes outer shelf, continental slope, and rise deposits of Mesozoic to Paleogene age, and a series of gneiss domes exposed along the axis of the Lhagoi Kangri (Hu et al., 2008; Cai et al., 2011). These domes are in fault contact with the overlying Tethys Himalaya sequence, and were mainly exhumed during the middle Miocene (e.g., Maluski et al., 1988; Chen et al., 1990). The Kangmar Dome, perhaps the best studied example, has a core of Cambrian orthogneiss mantled by Carboniferous and Permian metapelites overlain by low-grade Triassic metasedimentary rocks intruded by mafic and aplite dikes (Lee et al., 2000; Wagner et al., 2010). South of the Tethys Himalaya and comprised between the South Tibetan Detachment in the north and the Main Central Thrust in the south, the Greater Himalaya forms the axial core of the orogen, consisting of medium to locally high-grade metasedimentary rocks and Cambro-Ordovician orthogneiss (Aikman et al., 2008; Carosi et al., 2018). North of the Tethys Himalaya, the Indus-Yarlung suture zone includes mélange units (An et al., 2017) and the Cretaceous Xigaze forearc basin stratigraphically overlying the Yarlung-Tsangpo forearc ophiolite (An et al., 2014; Hu et al., 2016; Wang et al., 2017).

3. The Nianchu

The Nianchu is sourced from the northern slope of the Greater Himalaya and cuts northward across the Tethys Himalayan zone to eventually join the Yarlung Tsangpo near the Xigaze city. As the largest southern tributary of the middle reaches of the Yarlung Tsangpo, the Nianchu originates from the Noijinkangsang Glacier (90.20° E, 29.04° N, 5950 m above sea level) and flows for 217 km north-westward covering a drainage area of 11,130 km^2 (Fig. 2A). The upper reaches of the Nianchu catchment are narrow and steep (average gradient 9.6‰), whereas the lower reaches northwest of Gyangze are broad and open (average gradient 2.2‰). The largest tributary is the Chongbayongchu (length 105 km, drainage area 2864 km^2), also originating from the northern slope of the Greater Himalaya and flowing northward to join the Nianchu at Gyangze. Two major dams are built on the river for hydropower and flood regulation, the Manla reservoir (2001) at the confluence with the Nieru Tsangpo tributary, and the Chongbahu reservoir (1989) in the upstream reaches of the Chongbayongchu. The smaller Chusong reservoir (2000) was built on the Jiagaxiong tributary.

Climatic conditions in the Nianchu catchment are plateau semi-arid with humid summer and dry winter seasons. The period from June to September accounts for 90% of the annual precipitation (Yang et al., 2011), which is on average 430 mm at Xigaze (3836 m a.s.l.), 288 mm at Gyangze (4090 m a.s.l.), and much lower in the Chongbayongchu and Nieru Tsangpo catchments in the rain shadow of the high Himalayan range (Liu and Chen, 1995) (Fig. 2C). The average annual temperature is 4.7 °C at Gyangze and 6.3 °C at Xigaze (Zhou et al., 2009), usually below zero in winter and relatively warm in summer (average temperature 13 °C). Because of cold semiarid climate, the effect of chemical weathering on sand mineralogy can be considered as very minor.

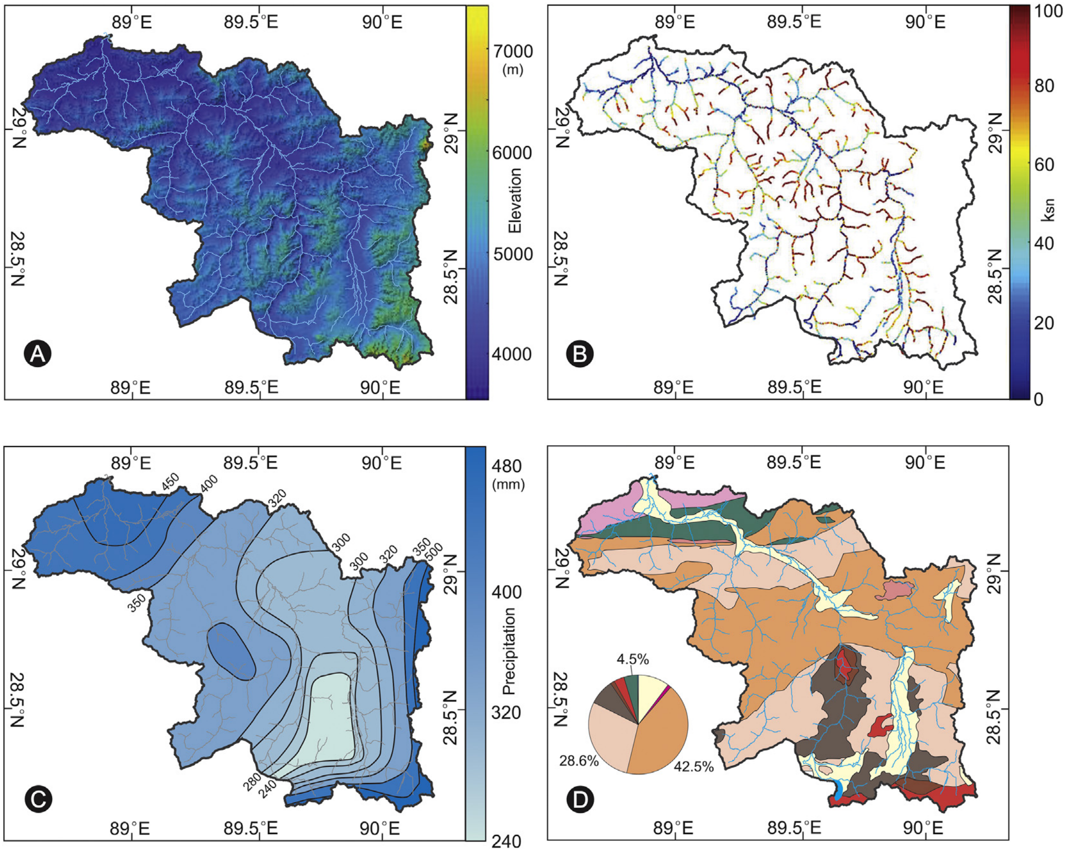

Fig. 2. Topography (A), channel steepness (B), precipitation (C), and relative distribution of geological units (D) in the Nianchu catchment. Relief and fluvial network are delineated in *TopoToolbox* from a 30-m-resolution digital elevation model provided by Advanced Spaceborne Thermal Emission and Reflection Radiometer (ASTER) global digital elevation model. Precipitation data after Liu and Chen (1995). The area of the Nianchu catchment was calculated with QGIS based on the 1:1500 000 geological map of Pan et al. (2004). Geological units as in Fig.1.

Wind storms are frequent in late winter to spring. The annual water discharge recorded at the Gyangze and Xigaze stations is 33 $m^3 s^{-1}$ and 51 $m^3 s^{-1}$, respectively; 65% of total discharge occurs in the wet season (Yang et al., 2011). The mean sediment concentration is 1.25 kg m^{-3}. The annual suspended load of the Nianchu measured at the Gyangze gauging station was estimated as 0.90×10^6 t a^{-1} (Guan et al., 1984) and 1.10×10^6 t a^{-1} (Liu, 1999) and at the Xigaze gauging station as 2.44×10^6 t a^{-1} in the 1980s and as 3.13×10^6 t a^{-1} in the 1990s (Li, 2001). The glaciated area (Fig. 1; 224 km^2) represents ~2% of the Nianchu catchment. Ice and snow melting in summer contribute largely to peak discharge, which occurs in August accounting for 24% of the annual flux. Summer floods may occur, whereas the river has lowest levels in winter when it commonly freezes.

3.1. Geology of the catchment

Tethys Himalayan sedimentary rocks represent 72% of the Nianchu catchment. The rest is accounted for by Quaternary cover (10%), Kangmar Dome and surrounding Paleozoic strata (9%), ophiolites, mélange, and forearc turbidites (5%), other igneous rocks (3%), and Proterozoic metamorphic rocks (1%) (Fig. 2D). The Greater Himalaya represents the largely snow-covered southernmost part of the catchment, with igneous and metamorphic rocks characterized by U-Pb zircon ages clustering around 500 Ma, 850 Ma, 1.1 Ga, 1.5–1.8 Ga, and 2.5–2.6 Ga (DeCelles et al., 2000, 2004; Gehrels et al., 2011). Paleozoic strata are exposed along the north-dipping Gyirong–Kangmar thrust (Ratschbacher et al., 1994), with the Chongbayongchu branch cutting across the orthogneiss core of the Kangmar Dome. Zircon ages in the Kangmar Dome cluster around 500 Ma (Lee et al., 2000; Wu et al., 2015), with much younger zircon rims dated between 30 Ma and 21 Ma (Hacker et al., 2011). The mainly Mesozoic sedimentary rocks of the Northern Tethys Himalaya yield zircon age spectra with three modes at 480–570 Ma, 750–1200 Ma, and 2430–2560 Ma (Gehrels et al., 2003, 2011). An additional minor cluster at 220–280 Ma may reflect foreign sediment provenance from either the Lhasa block (Li et al., 2010; Webb et al., 2013) or far-away sources in the Gondwanide orogen (Wang J. et al., 2016). The ophiolite sequence, formed at 125–130 Ma (Li et al., 2009; Hébert et al., 2012; Dai et al., 2013), is exposed along the Indus-Yarlung suture and is drained by the Qiangdui, Qiongrang and Zire tributaries. Strata in the Xigaze forearc basin yield mostly Cretaceous, some Jurassic, and a few older zircon ages (Wu et al., 2010; Aitchison et al., 2011; An et al., 2014).

4. Analytical methods

Twenty-one samples of fine-grained to coarse-grained sand were collected during the summers of 2013 and 2016 from active river bars, eight from the Nianchu trunk river and 13 from tributaries draining different geological domains. Another set of five samples draining forearc ophiolites exposed in adjacent drainage basins were also analyzed for heavy minerals. Information on sampling sites and the petrographic and heavy-mineral datasets are provided in Supplementary Tables S1, S2 and S3.

4.1. Framework petrography

Fourteen samples were prepared for the petrographic framework. For each bulk sand sample, a quartered fraction was impregnated with araldite and cut into a standard thin section stained with alizarine red to distinguish calcite from dolomite. On each thin section, 350 sand grains were counted for each sample under the microscope (Gazzi-Dickinson method; Ingersoll et al., 1984). Sand was classified by its three main components quartz (Q), feldspars (F), and lithic fragments (L), considered if >10% QFL (e.g., a sand sample is called litho-feldspatho-quartzose if Q > F > L > 10% QFL; Garzanti, 2016, 2019). The metamorphic indices MI or MI*, ranging respectively from 0 (detritus from sedimentary and volcanic rocks) or 100 (detritus from very low-grade metamorphic rocks) to 500 (detritus from high-grade metamorphic rocks; Garzanti and Vezzoli, 2003), were used to express the average rank of metamorphic rock fragments. Median grain size was also determined in thin section by ranking and visual comparison with sieved standards of ϕ/4 classes.

4.2. Heavy minerals

Twenty-one samples were prepared for heavy mineral analyses. Heavy minerals were separated with sodium polytungstate (~2.90 g cm^{-3}) from a quartered aliquot of the 32–500 μm class obtained by sieving, recovered by partial freezing with liquid nitrogen, and mounted on a glass slide with Canada balsam. For each sample, between 200 and 250 transparent heavy mineral grains were either grain-counted under the petrographic microscope with the area method, or point-counted at a suitable regular spacing to obtain real volume percentages (Galehouse, 1971). Raman spectroscopy was applied to check dubious grains (Andò and Garzanti, 2014; Lünsdorf et al., 2019). The sum of zircon, tourmaline, and rutile over total transparent heavy minerals (ZTR index of Hubert, 1962) provides information on the extent of recycling (Garzanti, 2017). The transparent heavy mineral concentration (tHMC), calculated as the volume percentage of transparent heavy minerals (Garzanti and Andò, 2007, 2019), ranges from very poor (0.1 ≤ tHMC <0.5), poor (0.5 ≤ tHMC <1) and moderately poor (1 ≤ tHMC <2), to moderately rich (2 ≤ tHMC <5) and rich (5 ≤ tHMC <10).

The Source Rock Density (SRD; g cm^{-3}) index, defined as the weighted average density of terrigenous grains, is used to estimate the average density of source rocks and to check for significant hydraulic-sorting modifications of sand composition (Garzanti et al., 2009).

4.3. Areal exposures and river morphometry

The areal exposure of each lithological unit exposed in the Nianchu catchment was calculated with QGIS using STRM DEM data and based on the 1:1500 000 geological map of Pan et al. (2004). The relief and fluvial network of Nianchu catchment were delineated in TopoToolbox (software shell implemented in MATLAB; Schwanghart and Scherler, 2014) from a 30-m-resolution digital elevation model provided by Advanced Spaceborne Thermal Emission and Reflection Radiometer Global Digital Elevation Model (ASTER GDEM; http://www.gdem.aster.ersdac.or.jp). The channel-steepness index k_s, used to measure the bedrock-channel response to differential rock uplift (Whipple and Tucker, 1999; Kirby et al., 2003), is defined according to the power-law relationship: $S = k_s A^{-\theta}$ (S: local channel slope; A: contributing drainage area; θ: concavity index; Flint, 1974). This equation assumes that other controls such as lithology, climate, flood hydrology, or sediment flux are negligible or sufficiently well constrained (Kirby et al., 2003; Whipple, 2004). The concavity index θ is the rate of change of local slope as a function of increasing drainage area, generally found to lie within a narrow range between 0.3 and 0.6 under a steady-state bedrock channel profile (Tucker and Whipple, 2002; Whipple, 2004). A normalized channel steepness index, k_{sn}, is calculated using a fixed reference concavity $\theta_{ref} = 0.45$ to compare channel slopes with markedly different drainage areas and concavities (Korup and Schlunegger, 2009).

4.4. Statistical tools

Relative sediment budgets (i.e., the relative amount of detritus contributed by different tributaries to the trunk river) were assessed by forward mixing models based on integrated bulk petrography and heavy mineral data on bedload sand following the method of Garzanti et al. (2012). The Aitchison distance was used to measure the goodness of fit between theoretical detrital modes of sediment supplied by different combinations of diverse end-member sources and the observed detrital mode of the trunk river sediment (Resentini et al., 2017). In order to improve the accuracy of calculations, we analyzed two replicate samples each for the Zire tributary and the Nianchu upstream of the Yarlung Tsangpo confluence.

Statistical/graphical techniques used to illustrate our petrographic and heavy-mineral datasets include the compositional biplot (Gabriel, 1971), which allows discrimination among multivariate observations (points) while shedding light on the mutual relationships among variables (rays). The length of each ray is proportional to the variance of the corresponding variable in the dataset. If the angle between two rays is close to 0°, 90° or 180°, then the corresponding variables are directly correlated, uncorrelated or inversely correlated, respectively.

4.5. Erosion rate calculations

The sediment yield (t a^{-1} km^{-2}) of a given source was calculated as the ratio of sediment flux (10^6 t a^{-1}) and the area of the source obtained from the digital geological map. The erosion rate (mm a^{-1}) is estimated by calculating the ratio between the sediment yield and the estimated average density of exposed source rocks.

5. Results

5.1. Modern sand of Nianchu tributaries

The Chongbayongchu carries feldspatho-litho-quartzose sedimentaclastic sand with plagioclase > K-feldspar, pelitic, sparitic, and metasedimentary lithic grains, and some plutonic rock fragments and mica (Figs. 3A, 4A, B). The poor to moderately poor heavy-mineral assemblage includes amphibole and garnet, associated with epidote, tourmaline, sillimanite, apatite, and clinopyroxene (Fig. 4C, Table 1). Common sillimanite and garnet in sample 16A047, where chloritoid is rare (Table 1), reflect a Greater Himalaya contribution. Metamorphic detritus from the Greater Himalaya is however subordinate, because of both limited exposure area (~3% of the catchment) and presence of the Manla and Chongbahu reservoirs that may have trapped part of the sediment flux generated in the headwaters. Sedimentary lithics thus prevail over metamorphic lithics, and metamorphic indices are very low (Table 1). Additional metamorphic detritus from the Kangmar gneiss dome is reflected by an only slight downstream increase in metamorphic lithics, metamorphic indices, mica (biotite ≈ muscovite), heavy-mineral concentration, epidote and chloritoid, but otherwise overwhelmed by a further increase of sedimentary to low grade metasedimentary grains including sparite (Table 1).

The Rilang and Danxiong tributaries, draining Mesozoic Tethys Himalayan strata, carry quartzo-lithic to litho-quartzose sand with dominant shale/slate, siltstone/metasiltstone, phyllite, and schist fragments (Figs. 3B, 4A, B). Their poor to moderately poor heavy-mineral suites mainly include garnet, amphibole, epidote and tourmaline, with minor clinopyroxene, chloritoid, apatite, zircon, and titanite (Fig. 4C, Table 1). The Sala tributary, mostly draining Jurassic strata, carries a moderately poor assemblage mainly including epidote, amphibole, tourmaline and garnet (Table 1).

Different to the Chongbayongchu, Rilang and Danxiong, the Qiangdui and Qiongrang tributaries, carry quartzo-lithic to feldspatho-quartzo-lithic ultramaficlastic sand dominated by serpentinite grains associated with metapelite, metasandstone, shale/slate, and metabasite rock fragments (Figs. 3C, 4A, B). Moderately rich heavy-mineral assemblages mostly include amphibole, clinopyroxene and epidote, with subordinate garnet, olivine, prehnite, apatite, chloritoid, tourmaline, and rare spinel and orthopyroxene (Fig. 4C, Table 1).

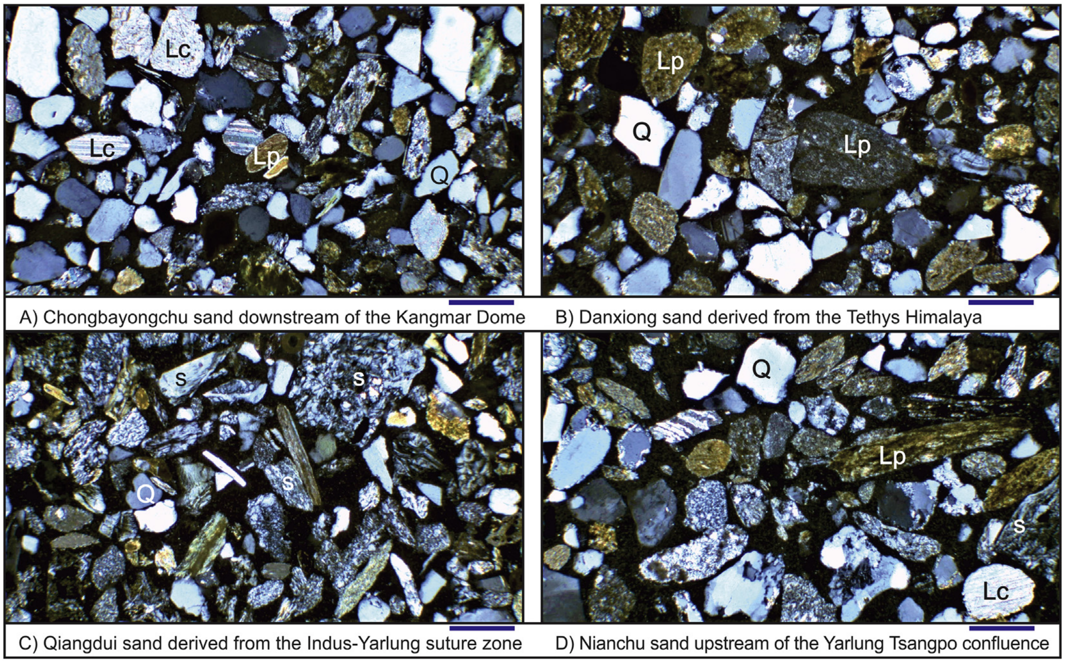

A) Chongbayongchu sand downstream of the Kangmar Dome

B) Danxiong sand derived from the Tethys Himalaya

C) Qiangdui sand derived from the Indus-Yarlung suture zone

D) Nianchu sand upstream of the Yarlung Tsangpo confluence

Fig. 3. Photomicrographs illustrating the variability of sand composition in the Nianchu catchment. (A) Litho-quartzose sand derived from the orthogneissic core and surrounding Paleozoic strata of the Kangmar dome; (B) litho-quartzose sedimentaclastic/low-rank metasedimentaclastic sand derived from weakly metamorphosed Mesozoic strata of the Tethys Himalaya; (C) quartzo-lithic sand with dominant serpentinite grains derived from forearc ophiolites of the Indus-Yarlung suture zone; (D) feldspatho-quartzo-lithic Nianchu sand. Q = quartz; Lc = carbonate, Lp = pelitic/low-rank metapelitic, and s = serpentinite rock fragments. All photos were taken with crossed polars; blue bar for scale is 250 μm.

The Zire tributary carries quartzo-lithic to litho-quartzose sand with sedimentary, metasedimentary lithics and serpentinite rock fragments (Fig. 4A, B), reflecting a provenance from both low-rank sedimentary rocks and ophiolite. The moderately rich transparent heavy-mineral assemblage includes mainly amphibole, clinopyroxene and epidote, associated with chloritoid, garnet, tourmaline, zircon, apatite, olivine, spinel, titanite and orthopyroxene (Fig. 4C, Table 1). The Qumei tributary carries a poor assemblage mainly consisting of epidote, amphibole, clinopyroxene, garnet, tourmaline and chloritoid (Table 1).

The SRD values (Supplementary Table S3) obtained for sand samples derived from Tethys Himalayan strata (SRD 2.56–2.67 g cm^{-3}) and partly supplied by forearc ophiolites (SRD 2.74–2.77 g cm^{-3}) are well within the range expected for the corresponding source rocks (Garzanti et al., 2009), indicating minor hydraulic sorting bias, if any.

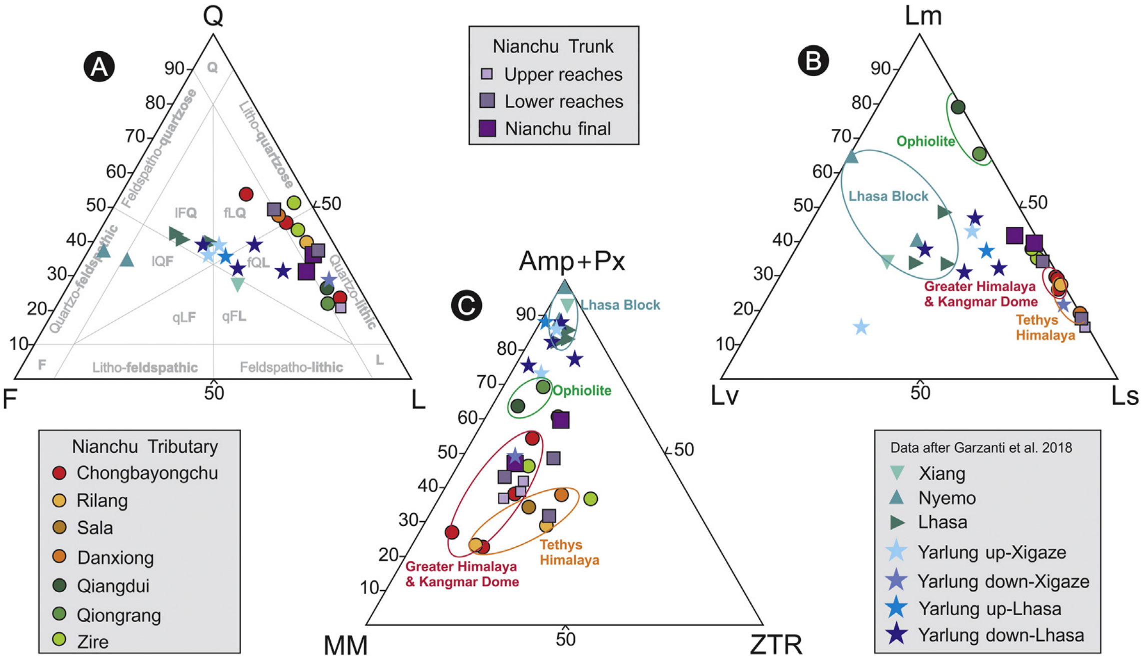

Fig. 4. Sand petrography (A, B) and heavy mineral assemblages (C). Data from Xiang, Nyemo, Lhasa and Yarlung Tsangpo sand after Garzanti et al. (2018). QFL diagram after Garzanti (2016, 2019). Q = quartz; F = feldspars; L = lithic grains (Lm = metamorphic; Lv = volcanic; Ls = sedimentary). ZTR = zircon + tourmaline + rutile; MM = chloritoid + garnet + staurolite + andalusite + kyanite + sillimanite; Amp = amphibole; Px = pyroxene.

Table 1
Petrographic and heavy-mineral data of Nianchu sand.

River	Sample	Q	KF	P	Lvm	Lsm	Lmfb	Lu	mica	HM	Total	MI*	MI
Greater Himalaya and dome													
Chongbayongchu	16A047	53	3	11	0.3	22	9	0	0.3	1	100	130	85
Chongbayongchu	16A048	43	3	5	0.1	30	12	0	3	3	100	196	148
Chongbayongchu	16A050	23	1	6	1	49	18	0	2	1	100	162	95
Mesozoic strata													
Rilang	S4682	39	2	5	1	38	14	0	1	0.3	100	110	63
Danxiong	16A057	46	3	6	0.1	34	6	1	0	3	100	136	47
Including ophiolite													
Qiangdui	16A056	25	1	7	0.3	13	9	40	1	6	100	134	101
Qiongrang	16A059	20	1	9	2	20	18	22	1	7	100	155	133
Other tributaries													
Zire	16A061	49	0	4	1	26	6	9	0.3	5	100	142	71
Zire	S4685	43	1	6	2	29	11	7	0.3	1	100	127	76
Trunk river													
Nianchu @upper reaches	16A051	20	2	5	0.3	59	11	0	1	0.3	100	142	45
Nianchu @lower reaches	16A055	36	1	4	0.1	46	10	0	1	2	100	140	55
Nianchu @lower reaches	16A060	47	2	7	1	24	8	5	1	4	100	128	74
Nianchu @final 1	S4686	35	1	6	1	33	13	9	0.3	2	100	135	81
Nianchu @final 2	16A062	30	2	9	3	30	20	3	0.3	2	100	141	105

River	Sample	tHMC	ZTR	Ttn	Ap	Ep	Grt	Cld	HgM	Amp	Px	OS	&HM	Total
Greater Himalaya and dome														
Chongbayongchu	16A047	0.8	7	1	10	8	33	0.5	19	15	7	0	0	100
Chongbayongchu	16A048	0.9	12	0.5	7	9	15	4	7	41	5	0	0.5	100
Chongbayongchu	16A049	1.7	14	3	5	17	14	15	4	22	6	0	0.4	100
Chongbayongchu	16A050	0.7	16	2	4	8	11	38	2	17	3	0	0	100
Mesozoic strata														
Rilang	16A046	0.5	23	4	8	15	16	10	3	14	7	0	0.4	100
Rilang	S4682	1.1	13	3	5	11	32	8	9	13	5	0	1	100
Sala	16A054	1.3	16	6	7	22	12	13	2	18	3	0.5	0	100
Danxiong	16A057	1.0	21	4	8	16	12	4	5	16	10	1	3	100
Including ophiolite														
Qiangdui	16A056	2.8	4	0	4	20	9	5	5	14	26	8	4	100
Qiongrang	16A059	3.2	6	0.4	3	28	4	8	1	34	8	3	4	100
Other tributaries														
Qumei	S4717	0.5	11	4	6	20	11	9	3	17	12	2	3	100
Zire	16A061	2.6	29	3	4	10	7	10	2	17	10	6	2	100
Zire	S4685	2.1	12	3	7	13	6	8	0.5	16	24	9	1	100
Trunk river														
Nianchu @upper reaches	16A051	0.3	13	2	9	22	8	18	1	12	14	2	0	100
Nianchu @upper reaches	16A052	0.7	12	1	9	18	9	21	3	14	12	1	0	100
Nianchu @upper reaches	16A053	0.4	13	2	9	18	12	11	3	10	18	1	1	100
Nianchu @lower reaches	16A055	0.8	23	3	6	16	11	15	3	17	6	0	0.4	100
Nianchu @lower reaches	16A058	0.9	9	4	4	19	21	7	2	15	15	3	1	100
Nianchu @lower reaches	16A060	1.4	15	1	7	21	4	14	1	24	8	1	2	100
Nianchu @final 1	S4686	1.3	14	3	5	14	4	11	1	23	21	1	2	100
Nianchu @final 2	16A062	1.6	10	1	1	13	17	11	0.5	13	21	10	2	100

Q = quartz; KF = K-feldspar; P = plagioclase; L = lithic grains (Lvm = volcanic and low-rank metavolcanic; Lsm = sedimentary and low-rank metasedimentary; Lmfb = high-rank metamorphic; Lu = ultramafic); HM = heavy minerals; MI* and MI = metamorphic indices (Garzanti and Vezzoli, 2003). tHMC = transparent heavy-mineral concentration; ZTR = zircon + tourmaline + rutile; Ttn = titanite; Ap = apatite; Ep = epidote-group minerals; Grt = garnet; Cld = chloritoid; HgM = staurolite + andalusite + kyanite + sillimanite; Amp = amphibole; Px = pyroxene; OS = olivine + spinel; &HM = other transparent heavy minerals (monazite, barite, vesuvianite, prehnite).

5.2. Modern Nianchu river sand

The Nianchu sand at Xigaze, just upstream of the Yarlung Tsangpo confluence, is feldspatho-quartzo-lithic and dominated by shale/slate and metasandstone grains associated with serpentinite, sparite, metafelsite and metabasite rock fragments (Figs. 3D, 4A, B). The moderately poor transparent heavy-mineral suite includes amphibole, clinopyroxene (mostly green augite), epidote, chloritoid, garnet and tourmaline, with minor olivine, zircon, enstatite, apatite, titanite, prehnite and Cr-spinel (Fig. 4C, Table 1).

In the upper reaches (Nieru Tsangpo), the sand is quartzo-lithic sedimentaclastic with dominant shale/slate and metasandstone grains (Fig. 4A, B). The very poor transparent heavy-mineral assemblage includes epidote, chloritoid, clinopyroxene (mostly green augite), amphibole, tourmaline, apatite and garnet (Fig. 4C, Table 1). Sand collected from the lower reaches upstream of the Indus-Yarlung suture zone displays a relative increase in quartz indicating a considerable supply from tributaries draining Mesozoic sedimentary and very-low-grade metasedimentary rocks of the Tethys Himalaya. Additional quartz is contributed by the Danxiong tributary. High-rank metamorphic rock fragments constantly decrease from the upper reaches to Nianchu final because of progressive dilution by sedimentary/metasedimentary and eventually ultramafic detritus (Fig. 4B). Downstream of the suture zone, the increase in ultramafic lithic grains at the expense of sedimentary lithic clasts, and of clinopyroxene, enstatite and olivine indicates significant local supply from the forearc ophiolites.

5.3. River morphometry

The Nianchu catchment shows a relatively homogeneous morphology. Although slope gradients are higher in the upper reaches than in the lower reaches, channel steepness remains in a narrow range for most stream segments ($60 < k_{sn} < 90$; Fig. 2B). The Nieru Tsangpo ($k_{sn} = 87$) and

Chongbayongchu ($k_{sn} = 79$) have relatively high steepness, whereas other tributaries display lower values ($k_{sn} \sim 60$) (Fig. 2B).

6. Detrital sources and Nianchu sand budget

6.1. Heavy mineral sources

In the Nianchu catchment, in particular sillimanite, garnet, chloritoid, enstatite, and olivine identify specific source-rock domains. Sillimanite, associated with garnet (sample 16A047), is shed from upper-amphibolite-facies metasedimentary rocks exposed in the upper tectonic levels of the Greater Himalaya. Metamorphic rocks surrounding the Kangmar Dome display a zonation from kyanite to chloritoid (Lee et al., 2000), which is particularly abundant (Sample 16A049, 16A050 and 16A051) in low-grade Mesozoic metapelites in the outer part of the dome. Enstatite and olivine are derived from ultramafic forearc ophiolites of the Indus-Yarlung suture zone.

Among other minerals, mostly augitic to diopsidic clinopyroxenes are supplied in limited amount not only from mafic rocks of the suture zone but also from mafic volcanic and volcaniclastic rocks interbedded or intruded in Triassic (Wang J. et al., 2016; Meng et al., 2019) and Cretaceous strata (Jadoul et al., 1998; Hu et al., 2008; Wang Y. et al., 2016).

6.2. End-members and provenance budget

The accurate definition of end-member sources, which are represented by either tributaries or specific geological domains, is an essential prerequisite to calculate a reliable provenance budget (Garzanti et al., 2012). The Chongbayongchu tributary, sourced in the Greater Himalaya and draining the Kangmar dome, provides information on the mineralogy of detritus shed from metamorphic rocks (Fig. 1B). Ultramafic lithic grains, olivine, enstatite, and Cr-spinel characterizing sand of the Qiangdui and Qiongrang tributaries offer indications on the ophiolite end-member. Unfortunately all five samples exclusively or mostly draining different lithospheric levels (mantle to diabase dykes and pillow lavas) of forearc ophiolites exposed in adjacent drainage basins yielded mixed heavy-mineral assemblages including large amounts of garnet or other minerals recycled from sedimentary strata, suggesting contamination by fine sand windblown during the dry season. A pure ophiolite end-member could thus not be obtained. Sand in the Rilang, Sala, and Danxiong tributaries, draining Mesozoic strata exclusively, best represents detritus derived from Tethys Himalayan strata.

The Nianchu sand in its final reach is dominantly supplied by Tethys Himalayan strata and subordinately by forearc-basin ophiolites and overlying strata. Contribution from the Greater Himalaya and Kangmar dome, significant in the upper reaches, is progressively diluted downstream (Fig. 5).

Forward mixing calculations suggest that the Zire tributary provides 30 ± 11% of total Nianchu sand flux, whereas the Qiongrang, Danxiong, Rilang plus Sala tributaries may each account for 15–20% of the total sand budget. Supply from the Chongbayongchu and Nieru Tsangpo headwater branches is limited to 11 ± 9% and 8 ± 8%, whereas other tributaries contribute very little (e.g., ~1% from the Qiangdui).

Sand collected in Qiangdui and Qiongrang tributaries consists of ophiolite and Mesozoic sedimentary detritus in similar proportions. The combined petrographic and heavy-mineral datasets (Table 1) indicate that most of the Nianchu sand (79 ± 10%) is generated from erosion of very low-grade Mesozoic strata of the Tethys Himalaya, with a subordinate but significant contribution from forearc ophiolites and overlying siliciclastic rocks (11 ± 8%) and limited supply from igneous and metamorphic rocks of the Greater Himalaya and Kangmar dome (9 ± 7%; Table 2).

The Nianchu sand provenance budget can be refined using the information available on age spectra of detrital zircon grains. The U-Pb age

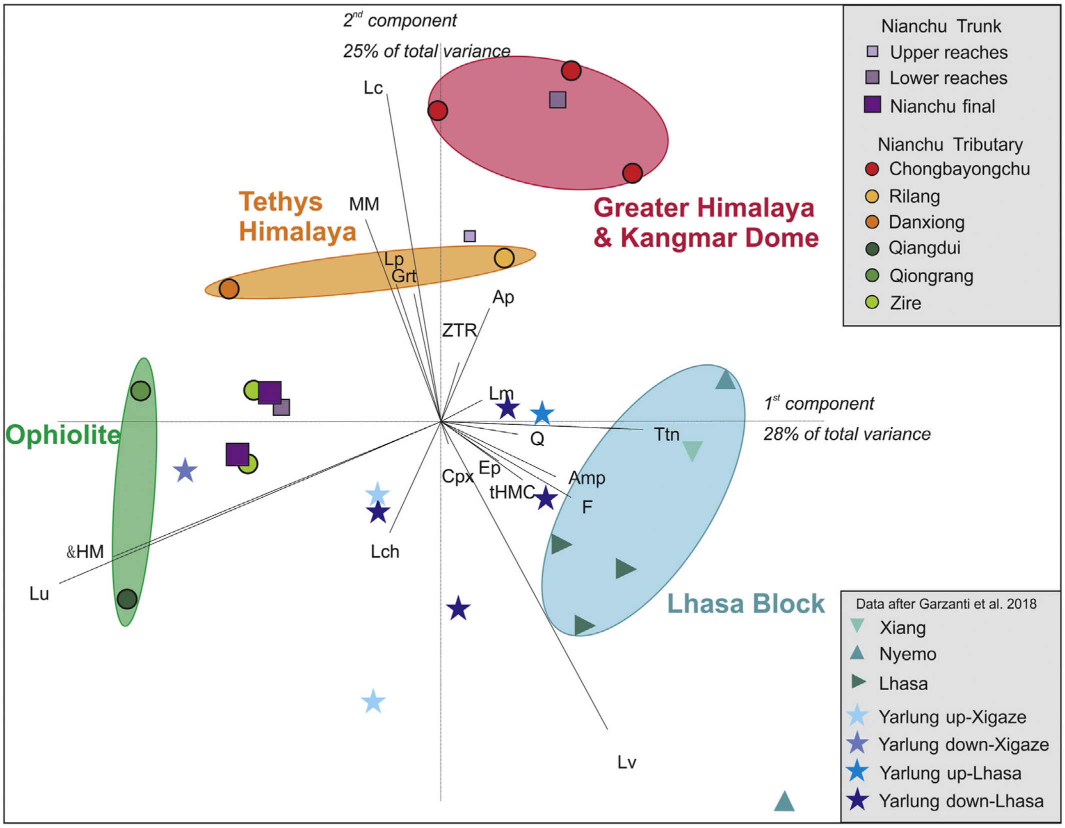

Fig. 5. Compositional biplot (Gabriel, 1971) based on all petrographic and mineralogical parameters. Data for Yarlung Tsangpo, Xiang, Nyemo, and Lhasa Rivers draining the Lhasa block after Garzanti et al. (2018). Lch = chert; other petrographic and heavy mineral parameters as in Table 1 and Fig. 3.

Table 2
Tentative sand provenance budget and erosion rates in Nianchu, Lhasa and middle Yarlung Tsangpo catchments. Provenance calculations are based on integrated forward mixing modeling considering bulk-petrography, heavy mineral, and zircon age data. Erosion rates are based on suspended sediment load measured at gauging stations.

	Nianchu						Yarlung Tsangpo	Lhasa
	Dome + Greater Himalaya	Tethys Himalaya	Suture zone	Total (Xigaze)	Upper Reaches (Gyangze)	Lower reaches	Middle Yarlung (Nugesha)	Total (Lhasa)
Contribution PTHM	**9%**	**79%**	**11%**					
	7%	*10%*	*8%*					
Contrib. age	>5%	<87%	8%					
Avg. contrib.	**9%**	**81%**	**10%**					
Area (%)	12%	83%	5%					
Area (km^2)	1336	9238	557	11,130	~6020	~5110	106,060	32,470
Suspended load (10^6 t a^{-1})	0.25	2.26	0.28	2.00–2.79	1.02	1.77	12.23	1.80
Sdm. load (10^6 t a^{-1})	0.28	2.49	0.31	2.20–3.07	1.12	1.95	13.45	1.98
Sdm. yield (t a^{-1} km^{-2})	207	269	552	198–276	186	381	127	61
SRD (g cm^{-3})	2.66	2.61	2.76	2.66	2.62	2.66	2.66	2.67
Erosion rate (mm a^{-1})	0.08	0.10	0.20	0.07–0.10	0.07	0.14	0.05	0.02

Note: Gauging stations are shown in Fig. 1; PTHM—petrography + heavy minerals; Sdm.—sediment; SRD—average grain density of analysed sand samples (Garzanti and Andò, 2007a); Mean values are in bold, and standard deviations in *italics*. Gyangze gauging station information after Guan et al. (1984) and Liu (1999); Xigaze, Lhasa gauging station information after Li (2001); Nugesha gauging station information after Shi et al. (2018). Bedload is considered as 10% of the suspended load.

distribution of zircon grains obtained from our same final Nianchu sample 16A062 displays three main peaks at ca. 500 Ma, 900 Ma and 1150 Ma, and minor clusters in the 53–200 Ma, and 2400–2800 Ma range (Guo et al., 2020). This geochronological data from Nianchu sand is consistent with the age distributions observed in the Xiabu (Carrapa et al., 2017) and Renbu rivers (Zhang et al., 2012) chiefly draining the Tethys Himalaya strata (Fig. 1B). Unlike the Xiabu River draining the Mabja Dome (Kouwu granite: 14.4 Ma; Kuday granite: 27.5 Ma; Zhang et al., 2004) and the Kampa Dome (Kampa leucogranite: 26.8–24.9 Ma; Liu et al., 2016), the Kangmar granite contains only a few newly grown zircons (Wu et al., 2015). This explains the lack of zircon grains younger than 50 Ma in Nianchu sand. All zircon grains younger than 200 Ma (8%) found in sample 16A062 were thus derived from forearc ophiolites (dated as 130–125 Ma; Li et al., 2009; Dai et al., 2013) or stratigraphically overlying forearc-basin turbidites (main age cluster at 130–80 Ma; Wu et al., 2010; Aitchison et al., 2011; An et al., 2014) exposed along the Indus-Yarlung suture zone. Because age spectra of detrital zircons are not markedly different in Greater Himalayan metamorphic rocks, Tethys Himalayan sedimentary rocks, and Kangmar gneiss dome (Lee et al., 2000; Gehrels et al., 2003, 2011), the much larger age population older than 200 Ma, accounting for about 92% of detrital zircons in sample 16A062 cannot be partitioned accurately among these three sources. Textural evidence, however, provides a clue useful to distinguish between first-cycle euhedral grains and recycled abraded grains. Most zircon grains in the Nianchu sand are rounded, and they thus appear to be largely recycled from siliciclastic Tethys Himalayan strata. Besides, at least 5% zircon grains aged between 670 and 1200 Ma are characterized by $Th/U < 0.1$ (Guo et al., 2020), suggesting an origin from metamorphic rocks (Hartmann and Santos, 2004) and thus provenance from the Kangmar Dome or Greater Himalaya.

Provenance budgets based on the age spectra of zircon grains are inevitably far less accurate than bulk-sediment provenance budgets, because zircon is only a rare accessory component, generally representing only ~0.02% of the sediment (Vezzoli et al., 2016; Garzanti et al., 2018), and because the zircon fertility of different end-member sources needs to be known and corrected for (Malusà et al., 2016; Malusà and Garzanti, 2019). The dominant zircon contribution from the Tethys Himalaya relative to other sources is also explained in the light of heavy-mineral analyses, which point out the notable differences in zircon concentration among different source rocks. Under the assumption of negligible hydraulic-sorting bias, an average zircon concentration of ~0.04% is indicated for Tethys Himalayan strata, which is notably higher than in samples derived partly from forearc rocks, Greater Himalaya, or Kangmar dome (Supplementary Table S2).

These considerations support the conclusions based on the integrated petrographic and heavy-mineral dataset, allowing us to refine our best estimate for sand generation in the Nianchu catchment, inferred to be ~81% recycled from the Tethys Himalayan zone, with subordinate supply from forearc rocks of the Indus-Yarlung suture zone (~10%) and from the Kangmar Dome + Greater Himalaya (~9%) (Table 2).

It is noteworthy that these values are similar to the percentage of the exposure areas of the corresponding geological domains (Table 2), which suggests – within the major uncertainties involved in our assessments – a similar sand-generation potential for all lithologies. The Tethys Himalaya thus provides, as expected, the bulk of the sand because of its wide exposure area. Our dataset apparently suggests a greater potential for sand generation only in the case of suture-zone ophiolites. However, this may be an artefact created by an underestimation of the extreme heavy-mineral concentration in dense mafic and ultramafic rocks. Conversely, the contribution from granitoid and metamorphic rocks exposed in the Greater Himalaya and Kangmar dome is apparently lower than expected, which may be partly ascribed to the presence of reservoirs in the Nianchu headwaters.

The petrographic and heavy-mineral signatures of Yarlung Tsangpo sand downstream of the Xigaze are similar to those of the Nianchu sand (Figs. 4, 5), which indicates a significant contribution from Tethys Himalayan rocks upstream. Suspended-load measurements in the Nugesha gauging station (Fig. 1) on the Yarlung Tsangpo, located 80 km downstream of the Nianchu confluence, suggest that supply from the Nianchu may account for as much as ~23% of Yarlung Tsangpo suspended load (Table 2).

7. Erosion rates and controlling factors

7.1. Sediment fluxes

The total sediment flux from a river catchment includes suspended load, which may be estimated from measurements in gauging stations, and bedload, which so far has proved to be too hard to measure directly and is thus generally roughly calculated as a proportion of the suspended load (e.g. 6%, Ferguson, 1984; ~10%, Summerfield and Hulton, 1994). Considering a bedload equal to 10% of suspended load and an average suspended load of ~2×10^6 t a^{-1} or 2.79×10^6 t a^{-1} as estimated by Shi et al. (2018) or measured at Xigaze gauging station (Li, 2001), the total Nianchu sediment flux can be constrained as $2.20–3.07 \times 10^6$ t a^{-1}, corresponding to a sediment yield of 198–276 t a^{-1} km^{-2}. Taking an average source-rock density of 2.66 g cm^{-3}, based on the SRD index of the Nianchu sand, the average erosion rate for the entire catchment is estimated as 0.07–0.10 mm a^{-1} (Table 2), which is consistent with the erosion rate assessed as <0.1 mm a^{-1} for southern Tibet by Garzanti et al. (2004).

Within the Nianchu basin, we can calculate, from suspended-load measurements carried out in the Gyangze gauging station (~10^6 t a^{-1}; Guan et al., 1984; Liu, 1999), an erosion rate of ~0.07 mm a^{-1} for the catchment upstream and of ~0.14 mm a^{-1} for the catchment downstream (Table 2).

Based on the Yarlung Tsangpo suspended load measured at Nugesha gauging station (Table 2), the average erosion rate for the entire middle Yarlung Tsangpo catchment is estimated at 0.05 mm a^{-1}, which is only half of the average erosion rate in the Nianchu catchment. An even lower average erosion rate (0.02 mm a^{-1}) (Table 2) is calculated for the Lhasa River catchment based on the flux of suspended sediment measured at Lhasa gauging station (Li, 2001).

Such low erosion rates, compared to the extremely rapid erosion across both the eastern and western Himalayan syntaxes, explain why the sediment contribution from dry southern Tibet to the Himalayan foreland basin is very minor (3% ± 2%: Garzanti et al., 2004, 2005; 1.5%: Shi et al., 2018).

7.2. Lithological versus climatic control on sand generation

If indeed a similar sand generation potential characterizes all diverse geological domains within the Nianchu basin, as suggested by the broad correspondence between exposure area and sediment supply from each, then we can readily draw general inferences on the relative effect of lithological and climatic control on erosion efficiency. The Tethys Himalaya sedimentary and very-low-grade metasedimentary rocks contain a greater proportion of shale and slate grains, which are prone to be comminuted to silt and clay particles preferentially entrained in suspension (McBride and Picard, 1987; Garzanti et al., 2013). Such mechanical comminution explains the much higher annual concentration of suspended sediment in the Nianchu (2.19 kg m^{-3} in 1980s, 2.55 kg m^{-3} in 1990s, Li, 2001) than in the Lhasa River catchment (0.15 kg m^{-3}, Guan et al., 1984; 0.13 kg m^{-3}, Li, 2001), where nearly half of the exposed bedrock is represented by tougher granitoids and volcanic rocks (Garzanti et al., 2018). The higher erodibility of sedimentary rocks (Morel et al., 2003) represents a most plausible explanation why average erosion rate is so notably higher in the Nianchu than in the Lhasa River catchment, even though the annual precipitation is less in the Nianchu basin (300–450 mm) than in the Lhasa River basin (450–500 mm) (Garzanti et al., 2018). Land use (Shi et al., 2018) and river channel morphology (Wang et al., 2015) are similar in the two regions and consequently cannot account for the discrepancy.

Moreover, if indeed the diverse geological domains have similar capacity to generate sand in the Nianchu basin, then the higher erosion rate by a factor of 2 in the lower reaches than in the upper reaches, where the slope gradient is much higher (Fig. 2B), would be best explained by the notably higher precipitation in the lower reaches (Fig. 2C) (Liu and Chen, 1995). The possibly less extensive land use (Zhang et al., 2010) and dominance of dam in the upper part of the river system may represent additional explanations.

8. Conclusions

The Yarlung Tsangpo (upper Brahmaputra River) flows along the Indus-Yarlung suture zone separating the former continental margins of India and Asia and receives detritus from both the Lhasa block in the north and the Himalaya in the south. The Nianchu River, as the major southern tributary of the Yarlung Tsangpo in the region, drains mainly Tethys Himalaya sedimentary and very-low-grade metasedimentary rocks, and carries quartzo-lithic to litho-quartzose sedimentaclastic/metasedimentaclastic sand with a few metamorphic, volcanic, and ultramafic lithic grains. The moderately poor heavy-mineral assemblage is mainly composed of amphibole, clinopyroxene and epidote, with minor garnet, sillimanite, chloritoid, olivine and enstatite, which are derived from different geological domains in the Nianchu catchment.

From the combination of high-resolution petrographic, heavy-mineral and detrital-geochronology datasets we could estimate that four fifths of total sediment in the Nianchu catchment are recycled from Tethys Himalayan strata, the rest being supplied in subequal proportions by forearc ophiolites and overlying siliciclastic rocks and by metamorphic rocks of the Greater Himalaya and Kangmar dome.

Mineralogical fingerprints of end-member sources, combined with gauged sediment fluxes, helped us to disentangle the interplay of lithological and climatic control on erosion patterns. Under the assumption that bedload is equal to 10% of suspended load, we could thus estimate for the Nianchu catchment an average erosion rate of about 0.10 mm a^{-1}. Lithological control explains the much higher erosion rate in the Nianchu catchment than in the Lhasa River catchment draining the Lhasa block to the north. Climatic control represents the most plausible reason why erosion rates surprisingly appear to be double in the lower Nianchu reaches than in the upper reaches despite the notably higher slope gradients. Sediment sequestration in artificial reservoirs and less extensive land use in the upper reaches represent additional explanations.

The petrographic, heavy-mineral, and geochronological signatures of Nianchu sand accurately defined in this study, especially as Tethys Himalayan source rocks are concerned, provide a useful reference for provenance studies based of ancient sandstones derived from the Himalayan orogen.

Acknowledgments

Heartfelt thanks to Xiumian Hu, Wei An, and Hanpu Fu who kindly provided most of the studied sand samples. Careful constructive reviews by Carita Augustsson and an anonymous reviewer are gratefully acknowledged. This study was supported financially by PRIN-MIUR (Progetto di Rilevante Interesse Nazionale, Ministero dell'Istruzione, dell'Università e della Ricerca) to E. Garzanti (2015EC9PJ5); MIUR – Dipartimenti di Eccellenza 2018–2022, Department of Earth and Environmental Sciences, University of Milano-Bicocca; Second Tibetan Plateau Scientific Expedition and Research Program (STEP, grant no. 2019QZKK0204) and State Scholarship Fund organized by China Scholarship Council (grant no. 201606450012). The authors declare no financial conflicts of interest.

Appendix A. Supplementary data

Supplementary data associated with this article can be found in the online version at https://doi.org/10.1016/j.sedgeo.2020.105604. These data include the Google map of the most important areas described in this article.

References

Aikman, A.B., Harrison, T.M., Lin, D., 2008. Evidence for early (>44 Ma) Himalayan crustal thickening, Tethyan Himalaya, southeastern Tibet. Earth Planet. Sci. Lett. 274, 14–23.

Aitchison, J.C., Xia, X., Baxter, A.T., Ali, J.R., 2011. Detrital zircon U–Pb ages along the Yarlung-Tsangpo suture zone, Tibet: implications for oblique convergence and collision between India and Asia. Gondwana Res. 20, 691–709.

An, W., Hu, X., Garzanti, E., BouDagher-Fadel, M.K., Wang, J., Sun, G., 2014. Xigaze forearc basin revisited (South Tibet): provenance changes and origin of the Xigaze Ophiolite. Geol. Soc. Am. Bull. 126, 1595–1613.

An, W., Hu, X., Garzanti, E., 2017. Sandstone provenance and tectonic evolution of the Xiukang Mélange from Neotethyan subduction to India–Asia collision (Yarlung-Zangbo suture, south Tibet). Gondwana Res. 41, 222–234.

Andò, S., Garzanti, E., 2014. Raman spectroscopy in heavy-mineral studies. In: Scott, R.A., Smyth, H.R., Morton, A.C., Richardson, N. (Eds.), Sediment Provenance Studies in Hydrocarbon Exploration and Production. Geological Society of London Special Publication 386, London, UK, pp. 395–412.

Bookhagen, B., Burbank, D.W., 2006. Topography, relief, and TRMM-derived rainfall variations along the Himalaya. Geophys. Res. Lett. 33, L08405. https://doi.org/10.1029/2006GL026037.

Burbank, D.W., Blythe, A.E., Putkonen, J., Pratt-Sitaula, B., Gabet, E., Oskin, M., Barros, A., Ojha, T.P., 2003. Decoupling of erosion and precipitation in the Himalayas. Nature 426, 652–655.

Burg, J.P., Leyreloup, A., Girardeau, J., Chen, G.M., 1987. Structure and metamorphism of a tectonically thickened continental crust: the Yalu Tsangpo suture zone (Tibet).

Mathematical and Physical Sciences. Philosophical transactions of the Royal Society of London. Series A 321, pp. 67–86.

Cai, F., Ding, L., Yue, Y., 2011. Provenance analysis of upper Cretaceous strata in the Tethys Himalaya, southern Tibet: implications for timing of India–Asia collision. Earth Planet. Sci. Lett. 305, 195–206.

Carosi, R., Montomoli, C., Iaccarino, S., 2018. 20 years of geological mapping of the metamorphic core across Central and Eastern Himalayas. Earth Sci. Rev. 177, 124–138.

Carrapa, B., Faiz bin Hassim, M., Kapp, P.A., DeCelles, P.G., Gehrels, G., 2017. Tectonic and erosional history of southern Tibet recorded by detrital chronological signatures along the Yarlung River drainage. Geol. Soc. Am. Bull. 129, 570–581.

Chen, Z., Liu, Y., Hodges, K.V., Burchfiel, B.C., Royden, L.H., Deng, C., 1990. The Kangmar Dome: a metamorphic core complex in southern Xizang (Tibet). Science 250, 1552–1556.

Dai, J., Wang, C., Polat, A., Santosh, M., Li, Y., Ge, Y., 2013. Rapid forearc spreading between 130 and 120 Ma: evidence from geochronology and geochemistry of the Xigaze ophiolite, southern Tibet. Lithos 172, 1–16.

DeCelles, P.G., Gehrels, G.E., Quade, J., Lareau, B., Spurlin, M., 2000. Tectonic implications of U-Pb zircon ages of the Himalayan orogenic belt in Nepal. Science 288, 497–499.

DeCelles, P.G., Gehrels, G.E., Najman, Y., Martin, A.J., Carter, A., Garzanti, E., 2004. Detrital geochronology and geochemistry of Cretaceous Early Miocene strata of Nepal: implications for timing and diachroneity of initial Himalayan orogenesis. Earth Planet. Sci. Lett. 227, 313–330.

DeCelles, P.G., Kapp, P., Gehrels, G.E., Ding, L., 2014. Paleocene-Eocene foreland basin evolution in the Himalaya of southern Tibet and Nepal: implications for the age of initial India-Asia collision. Tectonics 33, 824–849.

Ferguson, R.I., 1984. Sediment load of the Hunza River. In: Miller, K.J. (Ed.), The International Karakoram Project. Cambridge University Press, Cambridge, UK, pp. 581–598.

Flint, J.J., 1974. Stream gradient as a function of order, magnitude, and discharge. Water Resour. Res. 10, 969–973.

Gabriel, K.R., 1971. The biplot graphic display of matrices with application to principal component analysis. Biometrika 58, 453–467.

Galehouse, J.S., 1971. Point counting. In: Carver, R.E. (Ed.), Procedures in Sedimentary Petrology. Wiley, New York, pp. 385–407.

Gansser, A., 1980. The significance of the Himalayan suture zone. Tectonophysics 62, 37–52.

Garzanti, E., 2016. From static to dynamic provenance analysis – sedimentary petrology upgraded. Sediment. Geol. 336, 3–13.

Garzanti, E., 2017. The maturity myth in sedimentology and provenance. J. Sediment. Res. 87, 353–365.

Garzanti, E., 2019. Petrographic classification of sand and sandstone. Earth Sci. Rev. 192, 545–563.

Garzanti, E., Andò, S., 2007. Heavy-mineral concentration in modern sands: implications for provenance interpretation. In: Mange, M., Wright, D. (Eds.), Heavy Minerals in Use, Developments in Sedimentology Series 58. Elsevier, Amsterdam, pp. 517–545.

Garzanti, E., Andò, S., 2019. Heavy minerals for junior woodchucks. Minerals 9, 148. https://doi.org/10.3390/min9030148.

Garzanti, E., Vezzoli, G., 2003. A classification of metamorphic grains in sands based on their composition and grade. J. Sediment. Res. 73, 830–837.

Garzanti, E., Vezzoli, G., Andò, S., France-Lanord, C., Singh, S.K., Foster, G., 2004. Sand petrology and focused erosion in collision orogens: the Brahmaputra case. Earth Planet. Sci. Lett. 220, 157–174.

Garzanti, E., Vezzoli, G., Andò, S., Paparella, P., Clift, P.D., 2005. Petrology of Indus River sands: a key to interpret erosion history of the Western Himalayan syntaxis. Earth Planet. Sci. Lett. 229, 287–302.

Garzanti, E., Doglioni, C., Vezzoli, G., Ando, S., 2007a. Orogenic belts and orogenic sediment provenance. J. Geol. 115, 315–334.

Garzanti, E., Vezzoli, G., Andò, S., Lavé, J., Attal, M., France-Lanord, C., DeCelles, P., 2007b. Quantifying sand provenance and erosion (Marsyandi River, Nepal Himalaya). Earth Planet. Sci. Lett. 258, 500–515.

Garzanti, E., Andò, S., Vezzoli, G., 2009. Grain-size dependence of sediment composition and environmental bias in provenance studies. Earth Planet. Sci. Lett. 277, 422–432.

Garzanti, E., Resentini, A., Vezzoli, G., Andò, S., Malusà, M., Padoan, M., 2012. Forward compositional modelling of Alpine orogenic sediments. Sediment. Geol. 280, 149–164.

Garzanti, E., Limonta, M., Resentini, A., Bandopadhyay, P.C., Najman, Y., Andò, S., Vezzoli, G., 2013. Sediment recycling at convergent plate margins (Indo-Burman Ranges and Andaman-Nicobar Ridge). Earth Sci. Rev. 123, 113–132.

Garzanti, E., Limonta, M., Vezzoli, G., An, W., Wang, J., Hu, X., 2018. Petrology and multimineral fingerprinting of modern sand generated from a dissected magmatic arc (Lhasa River, Tibet). In: Ingersoll, R.V., Lawton, T.F., Graham, S.A. (Eds.), Tectonics, Sedimentary Basins, and Provenance: A Celebration of William R. Dickinson's Career. Geological Society of America Special Paper 540, pp. 197–221.

Gehrels, G., Kapp, P., DeCelles, P., Pullen, A., Blakey, R., Weislogel, A., Ding, L., Guynn, J., Martin, A., McQuarrie, N., Yin, A., 2011. Detrital zircon geochronology of pre-Tertiary strata in the Tibetan-Himalayan orogen. Tectonics 30, TC5016. https://doi.org/10.1029/2011TC002868.

Gehrels, G.E., DeCelles, P.G., Martin, A., Ojha, T.P., Pinhassi, G., Upreti, B.N., 2003. Initiation of the Himalayan orogen as an early Paleozoic thin-skinned thrust belt. Geological Society of America today 13, 4–9.

Godard, V., Bourlès, D.L., Spinabella, F., Burbank, D.W., Bookhagen, B., Fisher, G.B., Moulin, A., Léanni, L., 2014. Dominance of tectonics over climate in Himalayan denudation. Geology 42, 243–246.

Guan, Z., Chen, C., Qu, Y., 1984. Rivers and Lakes in Tibet. Science and Technology Press, Beijing (in Chinese).

Guo, R., Hu, X., Garzanti, E., Lai, W., Yan, B., Mark, C., 2020. How faithfully the geochronological and geochemical signatures of detrital zircon, titanite, rutile and monazite record magmatic and metamorphic events? A case study from the Himalaya and Tibet. Earth Sci. Rev. 103082. https://doi.org/10.1016/j.earscirev.2020.103082.

Hacker, B.R., Kylander-Clark, A., Lee, J., Cottle, J., Stearns, M., 2011. Laser-ablation split-stream petrochronology of Kangmar and Mabja north Himalayan gneiss domes. Journal of Himalayan Earth Sciences 44, 25–26.

Hartmann, L.A., Santos, J.O.S., 2004. Predominance of high Th/U, magmatic zircon in Brazilian Shield sandstones. Geology 32, 73–76.

Hauck, M.L., Nelson, K.D., Brown, L.D., Zhao, W., Ross, A.R., 1998. Crustal structure of the Himalayan orogen at ~90 east longitude from Project INDEPTH deep reflection profiles. Tectonics 17, 481–500.

Hébert, R., Bezard, R., Guilmette, C., Dostal, J., Wang, C., Liu, Z., 2012. The Indus–Yarlung Zangbo ophiolites from Nanga Parbat to Namche Barwa syntaxes, southern Tibet: first synthesis of petrology, geochemistry, and geochronology with incidences on geodynamic reconstructions of Neo-Tethys. Gondwana Res. 22, 377–397.

Hodges, K.V., 2000. Tectonics of the Himalaya and southern Tibet from two perspectives. Geol. Soc. Am. Bull. 112, 324–350.

Hu, X., Jansa, L., Wang, C., 2008. Upper Jurassic–Lower Cretaceous stratigraphy in south-eastern Tibet: a comparison with the western Himalayas. Cretac. Res. 29, 301–315.

Hu, X., Sinclair, H.D., Wang, J., Jiang, H., Wu, F., 2012. Late Cretaceous-Palaeogene stratigraphic evolution in the Zhepure Mountain of southern Tibet: implications for the timing of India-Asia initial collision. Basin Res. 24, 520–543.

Hu, X., Garzanti, E., Moore, T., Raffi, I., 2015. Direct stratigraphic dating of India-Asia collision onset at the Selandian (middle Paleocene, 59 ± 1 Ma). Geology 43, 859–862.

Hu, X., Garzanti, E., Wang, J., Huang, W., An, W., Webb, A., 2016. The timing of India-Asia collision onset–facts, theories, controversies. Earth Sci. Rev. 160, 264–299.

Hubert, J.F., 1962. A zircon–tourmaline–rutile maturity index and the interdependence of the composition of heavy mineral assemblages with the gross composition and texture of sandstones. J. Sediment. Petrol. 32, 440–450.

Ingersoll, R.V., 1990. Actualistic sandstone petrofacies: discriminating modern and ancient source rocks. Geology 18, 733–736.

Ingersoll, R.V., Bullard, T.F., Ford, R.L., Grimm, J.P., Pickle, J.D., Sares, S.W., 1984. The effect of grain size on detrital modes: a test of the Gazzi-Dickinson point-counting method. J. Sediment. Res. 54, 103–116.

Jadoul, F., Berra, F., Garzanti, E., 1998. The Tethys Himalayan passive margin from Late Triassic to Early Cretaceous (South Tibet). J. Asian Earth Sci. 16, 173–194.

Kirby, E., Whipple, K.X., Tang, W., Chen, Z., 2003. Distribution of active rock uplift along the eastern margin of the Tibetan Plateau: inferences from bedrock channel longitudinal profiles. J. Geophys. Res. Solid Earth 108, 2217. https://doi.org/10.1029/2001JB000861.

Korup, O., Schlunegger, F., 2009. Rock-type control on erosion-induced uplift, eastern Swiss Alps. Earth Planet. Sci. Lett. 278, 278–285.

Lavé, L., Avouac, J.P., 2001. Fluvial incision and tectonic uplift across the Himalayas of central Nepal. J. Geophys. Res. Solid Earth 106, 26561–26591.

Lee, J., Hacker, B.R., Dinklage, W.S., Wang, Y., Gans, P., Calvert, A., Wan, J., Chen, W., Blythe, A.E., McClelland, W., 2000. Evolution of the Kangmar Dome, southern Tibet: structural, petrologic, and thermochronologic constraints. Tectonics 19, 872–895.

Li, D., 2001. Initial analysis for water and soil moving distribution and its damage and difficulty of management in Tibet. Tibet Science and Technology 1, 21–24 (in Chinese, with English abstract).

Li, G., Liu, X., Alex, P., Wei, L., Liu, X., Huang, F., Zhou, X., 2010. In-situ detrital zircon geochronology and Hf isotopic analyses from Upper Triassic Tethys sequence strata. Earth Planet. Sci. Lett. 297, 461–470.

Li, J., Xia, B., Liu, L., Xu, L., He, G., Wang, H., Zhang, Y., Yang, Z., 2009. SHRIMP U-Pb dating for the Gabbro in Qunrang Ophiolite, Tibet: the geochronology constraint for the development of eastern Tethys basin. Geotecton. Metallog. 33, 294–298 (in Chinese, with English abstract).

Liu, T., 1999. Hydrological characteristics of Yarlung Zangbo river. Acta Geograph. Sin. 54 (Suppl. 1), 157–164 (in Chinese, with English abstract).

Liu, T., Chen, A., 1995. The characteristics of the precipitation of Nian-chu River basin. Journal of Chengdu University of Science and Technology 85, 12–18 (in Chinese, with English abstract).

Liu, X., Wu, F., Yu, L., Liu, Z., Ji, W., Wang, J., 2016. Emplacement age of leucogranite in the Kampa Dome, southern Tibet. Tectonophysics 667, 163–175.

Lünsdorf, N.K., Kalies, J., Ahlers, P., Dunkl, I., von Eynatten, H., 2019. Semi-automated heavy-mineral analysis by Raman spectroscopy. Minerals 9, 385. https://doi.org/10.3390/min9070385.

Malusà, M.G., Garzanti, E., 2019. The sedimentology of detrital thermochronology. In: Malusà, M.G., Fitzgerald, P.G. (Eds.), Fission-Track Thermochronology and its Application to Geology. Springer, Cham, Switzerland, pp. 123–143.

Malusà, M.G., Resentini, A., Garzanti, E., 2016. Hydraulic sorting and mineral fertility bias in detrital geochronology. Gondwana Res. 31, 1–19.

Maluski, H., Matte, P., Brunel, M., Xiao, X., 1988. Argon 39-argon 40 dating of metamorphic and plutonic events in the north and high Himalaya belts (southern Tibet-China). Tectonics 7, 299–326.

McBride, E., Picard, D.M., 1987. Downstream changes in sand composition, roundness and gravel size in a short-headed, high-gradient stream, northwestern Italy. J. Sediment. Res. 57, 1018–1026.

Meng, Z., Wang, J., Ji, W., Zhang, H., Wu, F., Garzanti, E., 2019. The Langjiexue Group is an in situ sedimentary sequence rather than an exotic block: constraints from coeval Upper Triassic strata of the Tethys Himalaya (Qulonggongba Formation). Sci. China Earth Sci. 62, 783–797.

Morel, P., Von Blanckenburg, F., Schaller, M., Kubik, P.W., Hinderer, M., 2003. Lithology, landscape dissection and glaciation controls on catchment erosion as determined by cosmogenic nuclides in river sediment (the Wutach Gorge, Black Forest). Terra Nova 15, 398–404.

Pan, G., Ding, J., Yao, D., Wang, L., 2004. Geological map of the Qinghai-Xizang (Tibet) plateau and adjacent areas (1:1,500,000). Chengdu Institute of Geology and Mineral

Resources, China Geological Survey. Chengdu Cartographic Publishing House, Chengdu, China (in Chinese).

Ratschbacher, L., Frisch, W., Liu, G., Chen, C., 1994. Distributed deformation in southern and western Tibet during and after the India-Asia collision. J. Geophys. Res. Solid Earth 99, 19917–19945.

Resentini, A., Goren, L., Castelltort, S., Garzanti, E., 2017. Partitioning the sediment flux by provenance and tracing erosion patterns in Taiwan. J. Geophys. Res. Earth Surf. 122, 1430–1454.

Schwanghart, W., Scherler, D., 2014. TopoToolbox 2 – MATLAB-based software for topographic analysis and modeling in Earth surface sciences. Earth Surface Dynamics 2, 1–7.

Sciunnach, D., Garzanti, E., 2012. Subsidence history of the Tethys Himalaya. Earth Sci. Rev. 111, 179–198.

Shi, X., Zhang, F., Lu, X., Wang, Z., Gong, T., Wang, G., Zhang, H., 2018. Spatiotemporal variations of suspended sediment transport in the upstream and midstream of the YarlungTsangpo River (the upper Brahmaputra), China. Earth Surf. Process. Landf. 43, 432–443.

Summerfield, M.A., Hulton, N.J., 1994. Natural controls of fluvial denudation rates in major world drainage basins. J. Geophys. Res. Solid Earth 99, 13871–13883.

Tucker, G.E., Whipple, K.X., 2002. Topographic outcomes predicted by stream erosion models: sensitivity analysis and intermodel comparison. J. Geophys. Res. Solid Earth 107, 2179. https://doi.org/10.1029/2001JB000162.

Vezzoli, G., Garzanti, E., Limonta, M., Andó, S., Yang, S., 2016. Erosion patterns in the Changjiang (Yangtze River) catchment revealed by bulk-sample versus single-mineral provenance budgets. Geomorphology 261, 177–192.

Wagner, T., Lee, J., Hacker, B.R., Seward, G., 2010. Kinematics and vorticity in Kangmar Dome, southern Tibet: testing midcrustal channel flow models for the Himalaya. Tectonics 29, TC6011. https://doi.org/10.1029/2010TC002746.

Wang, J., Wu, F., Garzanti, E., Hu, X., Ji, W., Liu, Z., Liu, Z., 2016b. Upper Triassic turbidites of the northern Tethyan Himalaya (Langjiexue Group): the terminal of a sediment-routing system sourced in the Gondwanide Orogen. Gondwana Res. 34, 84–98.

Wang, J., Hu, X., Garzanti, E., An, W., Liu, X., 2017. The birth of the Xigaze forearc basin in southern Tibet. Earth Planet. Sci. Lett. 465, 38–47.

Wang, Y., Gao, L., Zeng, L., Chen, F., Hou, K., Wang, Q., Zhao, L., Gao, J., 2016a. Multiple phases of Cretaceous mafic magmatism in the Gyangze-Kangma area, Tethyan Himalaya, southern Tibet. Acta Petrologica Sinica 32, 3572–3596 (in Chinese, with English abstract).

Wang, Z., Yu, G., Wang, X., Melching, C.S., Liu, L., 2015. Sediment storage and morphology of the Yalu Tsangpo valley due to uneven uplift of the Himalaya. Sci. China Earth Sci. 58, 1440–1445.

Webb, A.A.G., Yin, A., Dubey, C.S., 2013. U-Pb zircon geochronology of major lithologic units in the eastern Himalaya: Implications for the origin and assembly of Himalayan rocks. Geol. Soc. Am. Bull. 125, 499–522.

Whipple, K.X., 2004. Bedrock rivers and the geomorphology of active orogens. Annu. Rev. Earth Planet. Sci. 32, 151–185.

Whipple, K.X., Tucker, G.E., 1999. Dynamics of the stream-power river incision model: implications for height limits of mountain ranges, landscape response timescales, and research needs. J. Geophys. Res. Solid Earth 104, 17661–17674.

Willems, H., Zhou, Z., Zhang, B., Gräfe, K.U., 1996. Stratigraphy of the Upper Cretaceous and lower Tertiary strata in the Tethyan Himalayas of Tibet (Tingri area, China). International Journal of Earth Sciences Geologische Rundschau 85, 723–754.

Wu, F., Ji, W., Liu, C., Chung, S., 2010. Detrital zircon U–Pb and Hf isotopic data from the Xigaze fore-arc basin: constraints on TransHimalayan magmatic evolution in southern Tibet. Chem. Geol. 271, 13–25.

Wu, F., Liu, Z., Liu, X., Ji, W., 2015. Himalaya leucogranite: petrogenesis and implication to orogenesis and plateu uplift. Acta Petrologica Sinica 31, 1–36 (in Chinese, with English abstract).

Yang, D., Oyang, H., Zhou, C., Chen, C., 2011. Runoff characteristics of the Nyangqu River Basin on the Qinghai-Tibet Plateau. Resources Science 33, 1272–1277 (in Chinese, with English abstract).

Zhang, H., Harris, N., Parrish, R., Kelley, S., Zhang, L., Rogers, N., Argles, T., King, J., 2004. Causes and consequences of protracted melting of the mid-crust exposed in the North Himalayan antiform. Earth Planet. Sci. Lett. 228, 195–212.

Zhang, J., Yin, A., Liu, W., Wu, F., Lin, D., Grove, M., 2012. Coupled U-Pb dating and Hf isotopic analysis of detrital zircon of modern river sand from the Yalu River (Yarlung Tsangpo) drainage system in southern Tibet: constraints on the transport processes and evolution of Himalayan rivers. Geol. Soc. Am. Bull. 124, 1449–1473.

Zhang, X., Wang, X., Chen, C., 2010. Dynamic analysis of land use change in Nianchu river basin supported by RS&GIS. The 2nd International Conference on Information Science and Engineering. IEEE, New Jersey, pp. 3665–3668.

Zhou, C., Yang, W., Wu, L., Liu, S., 2009. Glacier changes from a new inventory, Nianchu river basin, Tibetan Plateau. Ann. Glaciol. 50, 87–92.

Zhu, D., Zhao, Z., Niu, Y., Mo, X., Chung, S., Hou, Z., Wang, L., Wu, F., 2011. The Lhasa Terrane: record of a microcontinent and its histories of drift and growth. Earth Planet. Sci. Lett. 301, 241–255.